Downloaded from orbit.dtu.dk on: Sep 07, 2022

DTU Library

Influence of Ti and Cr Adhesion Layers on Ultrathin Au Films

Todeschini, Matteo; Bastos da Silva Fanta, Alice; Jensen, Flemming; Wagner, Jakob Birkedal; Han, Anpan

Published in:
A C S Applied Materials and Interfaces

Link to article, DOI:
10.1021/acsami.7b10136

Publication date:
2017

Document Version
Peer reviewed version

Link back to DTU Orbit

Citation (APA):
Todeschini, M., Bastos da Silva Fanta, A., Jensen, F., Wagner, J. B., & Han, A. (2017). Influence of Ti and Cr Adhesion Layers on Ultrathin Au Films. *A C S Applied Materials and Interfaces*, *9*(42), 37374–37385. https://doi.org/10.1021/acsami.7b10136

General rights
Copyright and moral rights for the publications made accessible in the public portal are retained by the authors and/or other copyright owners and it is a condition of accessing publications that users recognise and abide by the legal requirements associated with these rights.

- Users may download and print one copy of any publication from the public portal for the purpose of private study or research.
- You may not further distribute the material or use it for any profit-making activity or commercial gain
- You may freely distribute the URL identifying the publication in the public portal

If you believe that this document breaches copyright please contact us providing details, and we will remove access to the work immediately and investigate your claim.

1
2
3
4
5
6
7
8
9
10
11
12
13
14
15
16
17
18
19
20
21
22
23
24
25
26
27
28
29
30
31
32
33
34
35
36
37
38
39
40
41
42
43
44
45
46
47
48
49
50
51
52
53
54
55
56
57
58
59
60

THE INFLUENCE OF Ti AND Cr ADHESION LAYERS ON ULTRA-THIN Au FILMS

Matteo Todeschini, Alice Bastos da Silva Fanta, Flemming Jensen, Jakob Birkedal Wagner, Anpan Han*

DTU Danchip/Cen, Technical University of Denmark, Ørsteds Plads, Building 347, 2800 Kgs. Lyngby, Denmark

KEYWORDS

Adhesion layer, thin-film nanostructure, thin-film adhesion, electron microscopy, nano-optics, nano-electronics.

1
2
3
4
5
6
7
8
9
10
11
12
13
14
15
16
17
18
19
20
21
22
23
24
25
26
27
28
29
30
31
32
33
34
35
36
37
38
39
40
41
42
43
44
45
46
47
48
49
50
51
52
53
54
55
56
57
58
59
60

ABSTRACT

Efficient adhesion of gold thin-films on dielectric or semiconductor substrates is essential in applications and research within plasmonics, metamaterials, 2D materials, and nano-electronics. As a consequence of the relentless downscaling in nanoscience and technology, the thicknesses of adhesion layer and over-layer have reached tens of nanometers, and it is unclear if our current understanding is sufficient. In this report, we investigated how Cr and Ti adhesion layers influence the nanostructure of 2 – 20-nm-thin Au films by means of high-resolution electron microscopy, complemented with atomic force microscopy and X-ray photoelectron spectroscopy. Pure Au films were compared to Ti/Au and Cr/Au bilayer systems. Both Ti and Cr had a striking impact on grain size and crystal orientation of the Au over-layer, which we interpret as the adhesion layer enhanced wetting of Au and the formation of chemical bonds between the layers. Ti formed a uniform layer under the Au over-layer. Cr inter-diffused with the Au layer forming a Cr-Au alloy. The crystal orientation of the Au layers was mainly [111] for all thin-film systems. The results showed that both adhesion layers were partially oxidized, and oxidation sources were scrutinized and found. A difference in bilayer electrical resistivity between Ti/Au and Cr/Au systems was measured and compared. Based on these results, a revised and more detailed adhesion layer model for both Ti/Au and Cr/Au systems was proposed. Finally, the implications of the results were analyzed, and recommendations for the selection of adhesion layers for nano-optics and nano-electronics applications are presented.

INTRODUCTION

The deposition of metal thin-film structures on dielectric or semiconductor substrates is important for plasmonics, multilayer structures for photonic applications, organic transistors, substrates for graphene growth, carbon nanotubes, 2D materials devices based on e.g. graphene and MoS_2, and nanopores[1,2]. Noble metals such as Au, Ag, and Pt are often used for these applications. Due to their low chemical reactivity,

they adhere poorly to the substrate, leading to phenomena like delamination, peeling, and time-dependent device performances deterioration.

To enhance adhesion, extremely thin *adhesion layers* are applied between the substrate and the noble metal films. The most used adhesion metals are Ti and Cr, but the advantages of the individual materials as adhesion layers are poorly understood. The simplified adhesion layer model usually used in the micro and nanofabrication community is shown in Fig. 1. In this model, the adhesion layer and the noble metal over-layer are deposited sequentially by physical vapor deposition, and are considered to be completely uniform and in perfect contact. Ti and Cr are known to be more chemically reactive than noble metals, and thereby increase the adhesion as they chemically bind to the substrate. However, the model does not include any layer-layer interaction. Moreover, it is considered to be independent of the thin-film thickness.

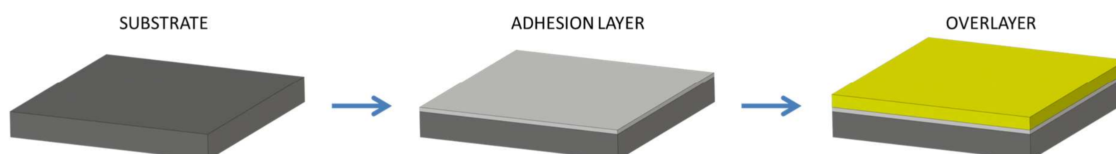

Figure 1. Schematic representation of a substrate, adhesion layer and over-layer system. The substrate is either a dielectric or semiconductor material and the over-layer is a metal.

In nanoscience and technology applications, the total metal thin-film thicknesses have reached tens of nanometers, and it is unclear if the simplified model is still adequate. As the over-layer thickness approaches the thickness of the adhesion layer, one might expect the latter to influence the nanostructure of the functional over-layer significantly. Furthermore, this influence might depend on the chemical properties of the adhesion layer. More importantly, the macroscopic properties of materials are strongly related to the microscopic structure. As an example, the thin-film nanostructure has a direct impact on the electrical conductivity, which is important in many nanoscience applications as introduced earlier. Polycrystalline metal thin-film electrical conductivity is lower than the bulk values, which is mainly

attributed to surface and grain boundary scattering[3,4,5]. It is unclear if the presence of an adhesion layer will have any influence on the thin-film electrical properties.

In this report, we investigate the influence of Ti and Cr adhesion layers on ultra-thin Au films deposited by electron beam evaporation at room temperature. Twelve samples (Table 1) were prepared and analyzed with complementary methods; transmission electron microscopy (TEM), atomic force microscopy (AFM), transmission Kikuchi diffraction (TKD), scanning TEM-energy dispersive x-ray spectroscopy (STEM-EDX), STEM-electron energy-loss spectroscopy (STEM-EELS), X-ray photoelectron spectroscopy (XPS) and micro four-point probe sheet resistance measurement (μ4PP). The paper is organized into four sections. First, a description of the growth, morphology and texture of pure Au films is reported. Second, the Au results are compared to an analysis of Ti/Au and Cr/Au bilayer systems. Profound differences in film morphology, texture, chemical composition, elemental diffusion and distribution, due to the adhesion layer presence, are observed and discussed. Third, the adhesion layer effect on the bilayer electrical resistivity of both systems is measured and compared. Finally, based on our results, we propose a revised and more detailed adhesion layer model for both Ti/Au and Cr/Au systems, together with the implications of the results and recommendations for the selection of adhesion layers for nano-optics and nano-electronics applications.

Sample (nominal thickness)	Label	Substrate		
		SiO_2	Si_3N_4 TEM grid	Si_3N_4
2 nm Au	2-Au	X		
20 nm Au	20-Au	X	X	
2 nm Ti and 2 nm Au	2-Ti/2-Au	X		
2 nm Ti and 20 nm Au	2-Ti/20-Au	X	X	X
2 nm Ti, 20 nm Au, 2 nm Ti and 20 nm Au	2-Ti/20-Au/2-Ti/20-Au			X
2 nm Cr and 2 nm Au	2-Cr/2-Au	X		
2 nm Cr and 20 nm Au	2-Cr/20-Au	X	X	X

Table 1. The samples analyzed in this study.

RESULTS AND DISCUSSION

Pure Au thin-films

We studied the growth process of a polycrystalline Au metal film through analysis of morphology and crystal orientation. The ultra-thin Au films were deposited by electron beam (e-beam) evaporation, and the deposition process was monitored by a mass calibrated QCM. For samples listed in Table 1, all nominal thicknesses were measured by QCM. Au has been chosen because of its extensive use in nanoscience and technology applications referenced in the introduction.

For the TEM bright field morphology analysis, Au thin-film cross section lamella samples were prepared by focused ion beam (FIB). During the sample preparation a layer of Pt and carbon film was deposited over the Au layer to protect the over-layer from FIB damage. From the cross section profile of the 2-Au sample (Fig. 2a), it is clearly visible that Au, when deposited directly on SiO_2, in order to reduce the interface energy, forms a nanoparticle-like layer in contrast to a continuous film. The diameter of the nanoparticles is about 10 nm. The nanoparticle morphology is confirmed by AFM analysis (Fig. S1a Supplementary). The RMS surface roughness is measured to 2.4 nm. For comparison, the RMS roughness of the SiO_2 substrate is 0.3 nm. When the thin-film nominal thickness is increased to 20 nm (20-Au sample, Fig. 2b), the Au layer becomes continuous, but a certain degree of surface roughness is still present due to coalescence of the different grains. The AFM image (Fig. S1b Supplementary) shows an RMS surface roughness of 1.0 nm, which is significantly lower than the 2-Au sample.

1 2 3 4 5 6 7 8 9 10 11 12 13 14 15 16 17 18 19 20 21 22 23 24 25 26 27 28 29 30 31 32 33 34 35 36 37 38 39 40 41 42 43 44 45 46 47 48 49 50 51 52 53 54 55 56 57 58 59 60

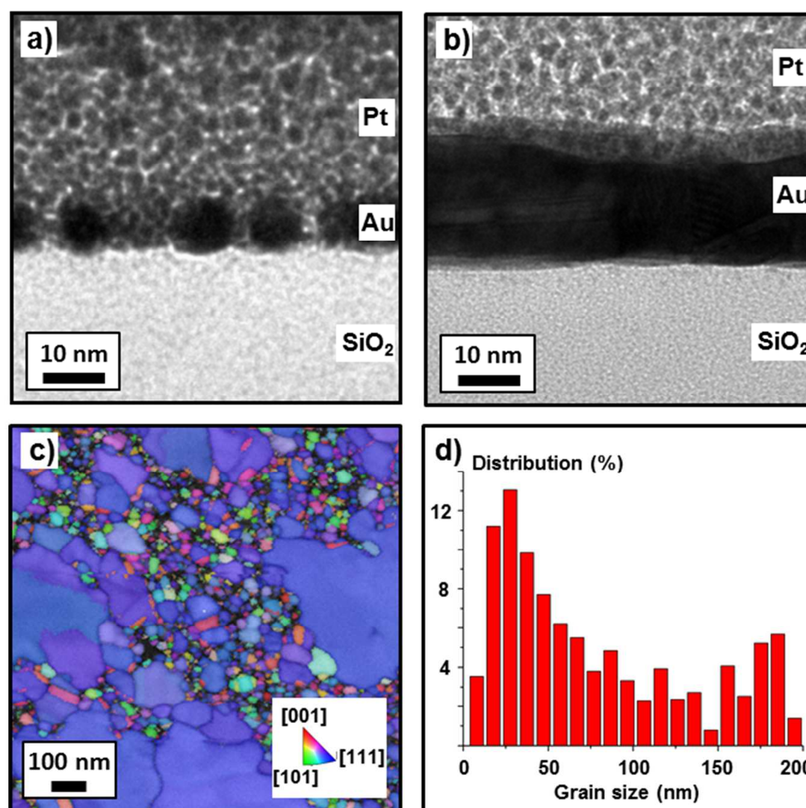

Figure 2. TEM cross section micrograph of the 2-Au sample (a) and the 20-Au sample (b). TKD inverse pole figure z-direction (IPFZ) map of the growth direction (c) and grain size distribution (d) of the 20-Au sample.

To investigate the crystal orientation of the metal thin-films, transmission Kikuchi diffraction (TKD) was used (Fig. 2c), allowing the visualization of crystal structure, crystallographic orientation and grain dimensions of thin films with a lateral resolution of 10 nm[6,7]. The nanostructure of the 20-Au film has a bimodal grain size distribution (Fig. 2d). While the smaller grains have different crystal orientations, the large grains (blue color) all have [111] orientation. An explanation of the TKD data follows (Fig. 3); growth of metal thin-films deposited by physical vapor deposition on amorphous dielectric substrates follow island growth[8,9]. For Au, which has a face-centered cubic unit cell, the (100) surface has a higher surface energy than the (111) surface, and to minimize energy, the (100) surface grows faster. Islands having (100) or (110) facets parallel to the substrate grow faster in the vertical direction, while islands with (111) facets parallel to the substrate grow faster laterally. The result is a continuous film, having laterally larger and flatter

islands with [111] crystal direction, and laterally smaller but taller islands with [100] and [110] orientations. More details about crystal growth are in the Supplementary Information (see thin-film crystal growth paragraph and Fig. S2 in Supplementary). For pure Au layers, our observations are consistent with the general consensus[10].

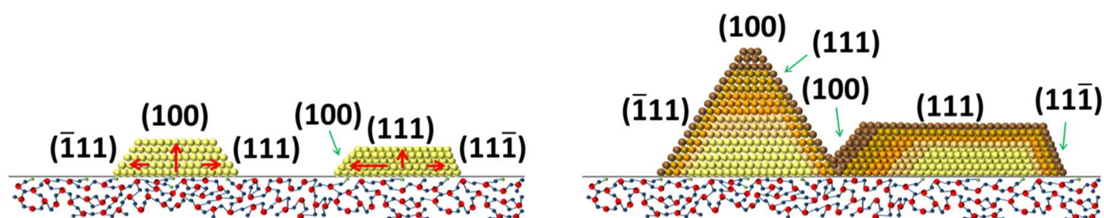

Figure 3. Schematic representation of metal thin-film growth of islands having different orientation with respect to the amorphous substrate surface. The {100} facets grow faster than {111} ones in order to decrease surface energy.

Ti/Au bilayer

To observe the influence of Ti in Ti/Au bilayer thin-film stacks, the Au thickness was kept the same as the samples in the pure Au section. From the TEM bright field cross section analysis of the 2-Ti/2-Au sample, it is observed that 2 nm of Ti forms a continuous layer below the Au layer (Fig. 4a). The Au layer is continuous over the Ti, indicating that Ti is responsible for an interface energy decrease, acting as an adhesive. The AFM analysis of the same sample confirms the continuous structure, and an RMS surface roughness of 0.8 nm is measured (Fig. S1c Supplementary). The 2-Ti/20-Au sample also shows a smoother film compared to the 20-Au sample (Fig. 4b), and the AFM analysis shows an RMS surface roughness of 0.5 nm (Fig. S1d Supplementary).

1
2
3
4
5
6
7
8
9
10
11
12
13
14
15
16
17
18
19
20
21
22
23
24
25
26
27
28
29
30
31
32
33
34
35
36
37
38
39
40
41
42
43
44
45
46
47
48
49
50
51
52
53
54
55
56
57
58
59
60

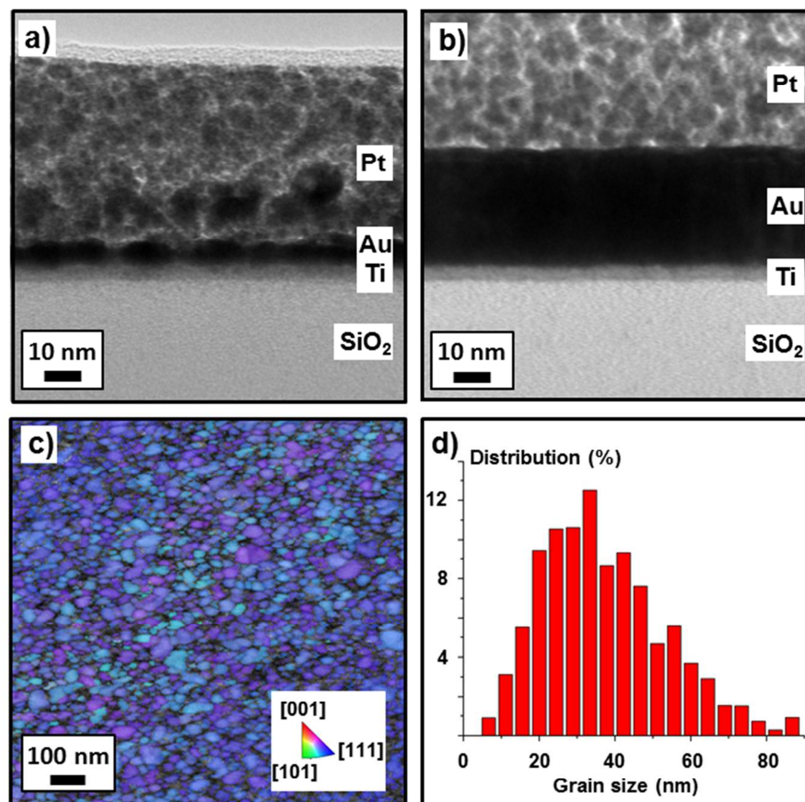

Figure 4. TEM cross section micrograph of the 2-Ti/2-Au sample (a) and the 2-Ti/20-Au sample (b). TKD inverse pole figure z-direction (IPFZ) map of the growth direction (c) and grain size distribution (d) of the 2-Ti/20-Au sample.

As visible in the TKD image (Fig. 4c), the addition of Ti has a profound impact on both grain size and orientation of the Au film. The image shows small grains mainly oriented in the [111] crystal direction, with an average grain size of 40 nm (Fig. 4d). The smaller grain size is attributed to an enhanced wetting of the deposited Au promoted by the Ti adhesion layer. The enhanced wetting behaviour increases the number of nucleation sites compared to the pure Au film case, where Au is evaporated directly onto the SiO_2 surface. This eventually leads to a much denser nucleation of the Au grains, which at the same time facilitates the inter-diffusion of Au atoms. The enhanced wetting might be due to the formation of Ti-Au bonds[11,12]. Carefully reviewing the literature, we found that the use of various wetting layers for the growth of smooth ultra-thin layers of Ag has been reported[13–16]. Ag is another noble metal with a similar chemical reactivity to Au. The studies show that the wetting layers act as substrates with an elevated density of heterogeneous

nucleation sites for the deposited Ag atoms, and that finely dispersed oxide defects represent the nucleation seeds for the nucleation.

The very dominant [111] crystal orientation observed in the Ti/Au case implies a decrease of the energy barrier for the formation of the energetically most favourable Au crystal structure. This is promoted by the denser nucleation and stronger inter-diffusion of Au atoms described above. In contrast to the pure Au case, all the grains have the same diffusion rate of the (111) exposed planes, and therefore the grains grow with a narrow grain size distribution. Since the film has been deposited at room temperature, the system did not have enough energy to overcome the energy barrier for grain coalescence, hence resulting in grains with a small average size.

The limited TKD resolution does not allow us to index grains smaller than 3 nm, which are shown as black areas in the map. In those areas grains having [100] and [110] crystal directions might be present, but are not visible due to their small grain size.

To investigate the crystallinity of the metal thin films, a high resolution (HR) TEM cross section investigation was performed (Fig. S3 Supplementary Information). The fast Fourier transform (FFT) suggests that the Ti layer is amorphous and the Au to be crystalline.

The chemical distribution of the Ti and Au elements in the bilayer system was investigated with STEM-EDX. For the 2-Ti/2-Au sample, the measurements at the Ti/Au interface show the presence of a continuous Ti layer below the Au layer (Fig. 5a). This result is in good agreement with the TEM micrograph of Fig. 4a. To verify the chemical composition of the sample, in particular to detect a possible presence of oxygen in the Ti layer, STEM-EELS analysis was used. A line scan across the layer interfaces (Fig. 5b) shows the presence of a Ti core loss L_3 edge at 460 eV and an L_2 edge at 465 eV. A SiO_2 O-K edge is visible at 538 eV, while the O-K edge of O bounded to Ti is found at 532 eV. The presence of oxygen in the Ti layer explains its amorphous structure: the oxygen binding to Ti atoms, disrupts the crystalline hexagonal close-packed structure of the pure metal. The Au layer has a crystalline structure for the same thickness as Ti. This is consistent with Au being deposited in a pure metallic form.

1
2
3
4
5
6
7
8
9
10
11
12
13
14
15
16
17
18
19
20
21
22
23
24
25
26
27
28
29
30
31
32
33
34
35
36
37
38
39
40
41
42
43
44
45
46
47
48
49
50
51
52
53
54
55
56
57
58
59
60

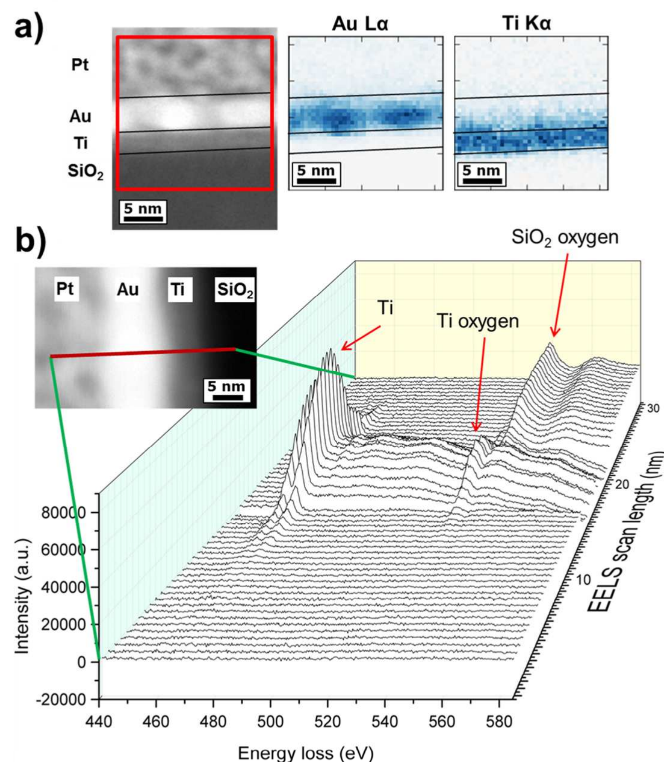

Figure 5. (a) STEM-EDX map of the 2-Ti/2-Au sample. Au Lα signal is acquired at 9713 eV, Ti Kα signal at 4510.9 eV. The map shows a continuous Ti layer below Au. (b) STEM-EELS linear scan of the 2-Ti/2-Au sample. The scan shows the presence of oxygen in the Ti layer.

The source of oxidation of the Ti layer can have three origins: i) oxidation due to migration of oxygen from the SiO_2 substrate, ii) oxidation during the e-beam deposition process, or iii) oxidation due to substrate contamination with water and oxygen molecules. To investigate the oxidation origin, XPS depth profile analysis were performed on as-deposited samples. Two XPS experiments were done. The first analysis was performed to clarify if oxygen is originating from source i). To rule out possible oxygen migration from the oxygen-rich SiO_2 substrate, the metal thin-films were deposited on amorphous Si_3N_4. For the 2-Ti/20-Au sample, after Ar ion milling of 20 nm of Au, the Au 4f signal intensity decreases (Fig. 6a) and Ti 2p and O 1s signals start to appear (Fig. 6b and 6c).

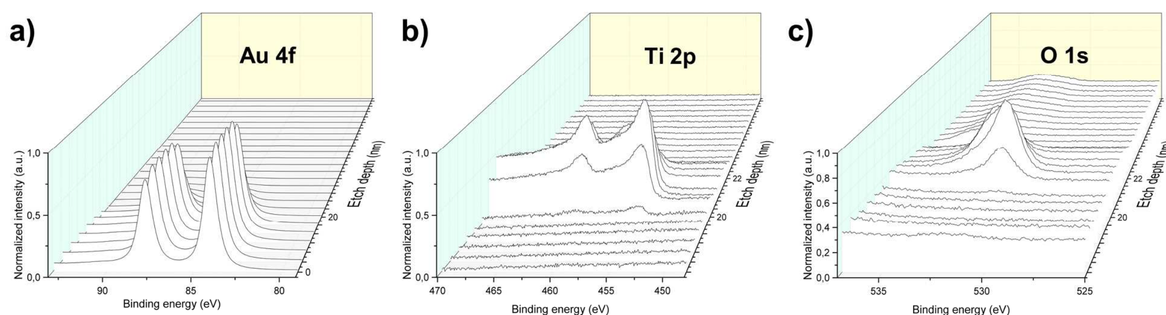

Figure 6. XPS peaks of the 2-Ti/20-Au sample XPS depth profiling on Si_3N_4 substrate. From the surface to a depth of 20 nm, only the Au 4f signal is visible (a). XPS signals from deeper than 20 nm show the Au signal decrease and both Ti 2p (b) and O 1s (c) signals appear.

A peak fit for the Ti signal was performed, and is reported in Fig. S4 of Supplementary Information. The Ti 2p peak is a convolution of three components: a TiN doublet at 455.0 and 461.1 eV, a TiO_2 doublet at 457.7 and 464.0 eV and a TiO_x signal, which forms the descending background tail[17]. The fit gives the following information: 1) Ti has formed Ti-N bonds with the Si_3N_4 substrate; 2) the adhesion layer is partially oxidized during deposition and not from source i). Metallic Ti could not be detected here, but its presence cannot be excluded: metallic Ti is highly reactive with respect to oxygen and nitrogen, and the destructive sputtering process used for the depth profiling could have enhanced the mixing between Ti, O and N, catalyzing the reaction of the metallic Ti bound to Au to form an oxide or a nitride.

The second analysis investigated whether the oxygen is originating from source ii) or iii). A 2-Ti/20-Au/2-Ti/20-Au sandwich structure was deposited and analyzed. The result is shown in Fig. S5 of Supplementary Information. Both layers of titanium are partially oxidized: the Ti 2p peak signals (Fig. S5a Supplementary) are present together with O 1s signal (Fig. S5b Supplementary).

The O 1s signal in the Ti layer in contact with the Si_3N_4 substrate has higher intensity than the one of the Ti layer between the Au layers. Hence, the Ti layer in contact with the substrate is more oxidized, which suggests that Ti reacts with water adsorbed on the substrate surface. We conclude that the oxygen originates from sources ii) and iii). Water is present in thin-film deposition instruments, and it is very difficult to remove because of its capacity to form hydrogen bonding with many materials. Ti reacts with water and oxygen and forms titanium oxides. Based on the above we propose an explanation for the Ti

1
2
3
4
5
6
7
8
9
10
11
12
13
14
15
16
17
18
19
20
21
22
23
24
25
26
27
28
29
30
31
32
33
34
35
36
37
38
39
40
41
42
43
44
45
46
47
48
49
50
51
52
53
54
55
56
57
58
59
60

promoted enhanced adhesion. Ti is highly reactive and reacts chemically both with the substrate and the Au over-layer. As our measurements show the Ti layer is only partially oxidized leading to a good adhesion. A complete oxidation would have passivated the Ti surface with only oxygen terminations, preventing the formation of Ti-Au bonds and leading to poor adhesion.

We do not observe inter-diffusion of Ti into Au at room temperature. Our results agree with previous work by Masahiro et al., which reported that no Ti-Au inter-diffusion is observed below 175°C using Auger electron spectroscopy (AES), X-ray and electron diffractometry[18]. At high deposition temperatures, however, several groups have reported Ti-Au inter-diffusion[19,20]. To limit the Ti-Au inter-diffusion above 200°C, the most adopted solution is the use of diffusion barriers like Pd[19] and Pt[21,22].

Cr/Au bilayer

Different to the case with the Ti adhesion layer, TEM bright field analysis of the 2-Cr/2-Au sample shows a single continuous layer (Fig. 7a). The AFM RMS surface roughness is 1.2 nm (Fig. S1e Supplementary Information). Increasing the nominal Au thickness to 20 nm for the 2-Cr/20-Au sample, the film still presents a single-layer morphology (Fig. 7b), while the RMS surface roughness decreases to 0.6 nm (Fig. S1f Supplementary Information). The addition of Cr has an impact on grain size and orientation of Au (Fig. 7c). The TKD result shows a uniform texture, where almost all grains are oriented in the [111] crystal direction. The average grain size is 36 nm (Fig. 7d). Prior STM studies showed that the presence of Cr leads to a roughness reduction of the Au surface[23]. The roughness reduction is confirmed by our investigation. As for Ti, when Cr is used as adhesion layer the Au forms smaller grains compared to pure Au. The same explanation as reported for Ti can be applied: Cr behaves as a wetting layer for the subsequently deposited Au. The wetting behaviour increases the number of nucleation sites and also decreases the energy barrier for the formation of the most densely packed and energetically favourable Au [111] crystal orientation, which grows with a narrow grain size distribution. In this case, also small grains with [100] and [110] crystal orientations have been detected. This might suggest that for Au on Cr the [111] orientation is energetically

1
2
3
4
5
6
7
8
9
10
11
12
13
14
15
16
17
18
19
20
21
22
23
24
25
26
27
28
29
30
31
32
33
34
35
36
37
38
39
40
41
42
43
44
45
46
47
48
49
50
51
52
53
54
55
56
57
58
59
60

less favored with respect to the [100] and [110] orientations compared to the Ti/Au case. The same considerations about chemical reactivity with respect to Au reported for Ti can be applied to Cr, as both are transition metals with a very similar electron configuration.

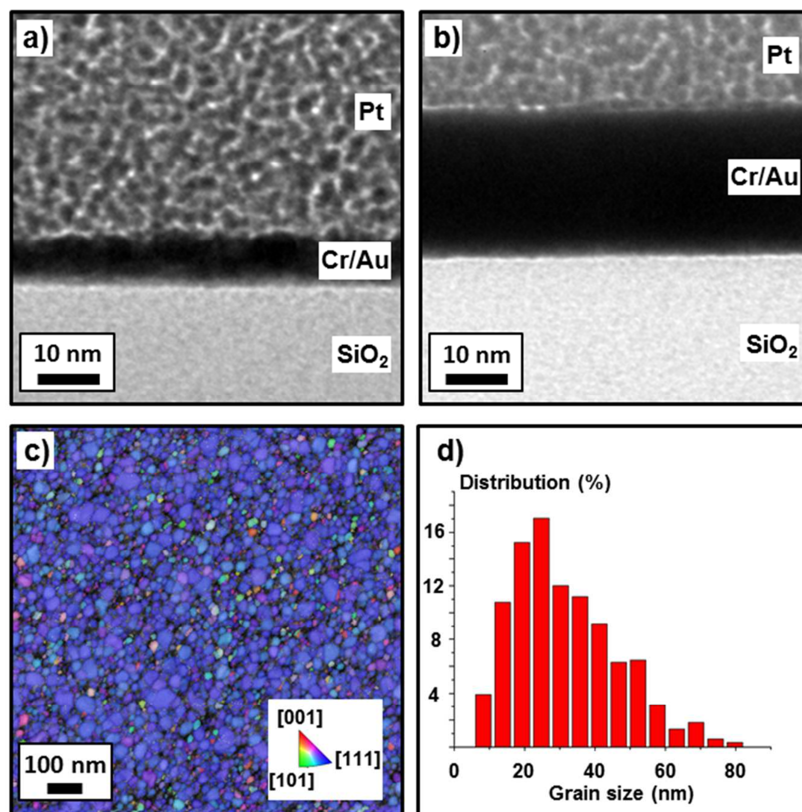

Figure 7. TEM cross section micrograph of the 2-Cr/2-Au sample (a) and the 2-Cr/20-Au sample (b). TKD inverse pole figure z-direction (IPFZ) map of the growth direction (c) and grain size distribution (d) of the 2-Cr/20-Au sample.

The Cr and Au elemental distribution inside the single-layer structure is studied by means of STEM-EDX. The analysis of the 2-Cr/2-Au sample shows the presence of Cr throughout the whole thickness of the Au layer (Fig. 8a). Since Cr and Au were deposited sequentially and not by a co-deposition process, this result suggests a strong inter-diffusion. The oxidation state of the adhesion layer for the same sample was analyzed with STEM-EELS (Fig. 8b). The analysis shows a Cr L_3 edge at 585 eV and an L_2 edge at 594 eV. The SiO_2 O-K edge is visible at 545 eV, while at 540 eV a weak O_{Cr}-K edge of O bounded to Cr is visible for a limited thickness below Au. Furthermore, the Cr edge presents a compositional tail along the scan

1
2
3
4
5
6
7
8
9
10
11
12
13
14
15
16
17
18
19
20
21
22
23
24
25
26
27
28
29
30
31
32
33
34
35
36
37
38
39
40
41
42
43
44
45
46
47
48
49
50
51
52
53
54
55
56
57
58
59
60

direction, giving confirmation of its diffusion into the Au layer. For the length of the tail there is no presence of O_{Cr}-K edge, indicating that Cr inside Au is in metallic form. This is in good agreement with the observed diffusion, which involves only metallic Cr. A STEM-EDX analysis was performed also for the 2-Cr/20-Au sample (Fig. 9). In this case it appears that the inter-diffusion between the elements is incomplete. However, the inter-diffusion is present for a thickness of 2-3 nm, suggesting that the diffusion process is limited to such a thickness when the materials are deposited at room temperature.

A 2-Cr/20-Au sample deposited on amorphous Si_3N_4 was analyzed by XPS depth profiling to investigate the oxidation origin of Cr. The depth profiling reveals that the Au 4f signal intensity starts to decrease (Fig. 10a), while the Cr 2p and O 1s signals start to appear after Ar milling of 20 nm Au (Fig. 10b and 10c, respectively). Due to the lower spatial resolution of XPS with respect to STEM-EDX, it is not possible to verify the thickness of Cr-Au inter-diffusion in this case. The XPS electron escape depth at 1486.7 eV for Au is around 15 Å[24], meaning that it is not possible to obtain information about inter-diffusion for layers thinner than this value without collecting a signal from the underlying material.

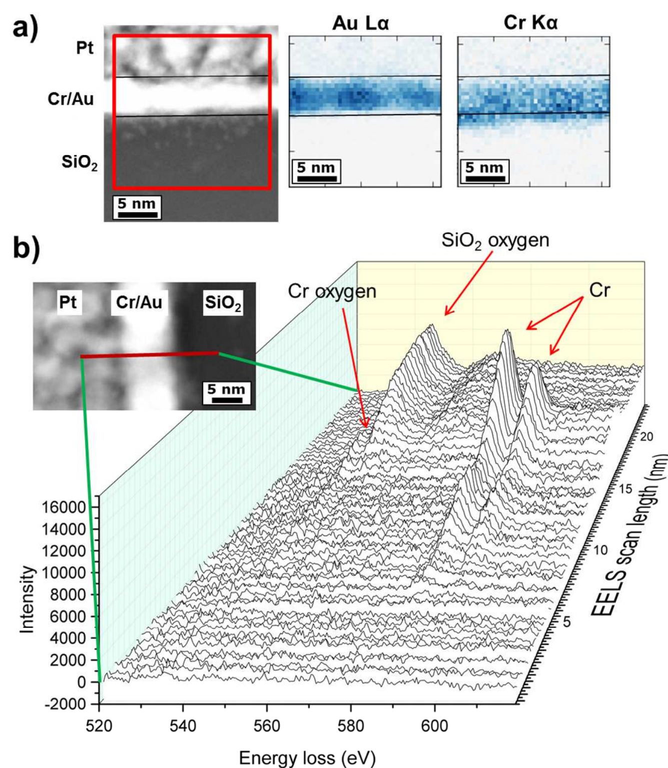

Figure 8. (a) STEM-EDX map of the 2-Cr/2-Au sample. Au Lα signal is acquired at 9713 eV, Cr Kα signal at 5414.7 eV. The map shows strong inter-diffusion between Cr and Au. (b) STEM-EELS linear scan of the 2-Cr/2-Au sample, which shows the presence of oxygen that is bounded to Cr, and Cr diffusion into the Au layer.

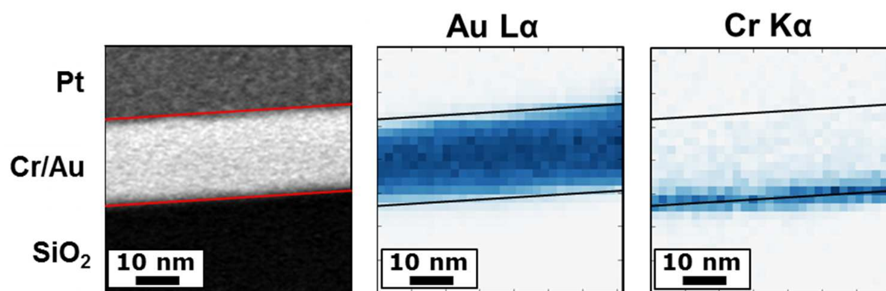

Figure 9. STEM-EDX map of the 2-Cr/20-Au sample. The map shows an inter-diffusion between Cr and Au for a thickness of 2-3 nm.

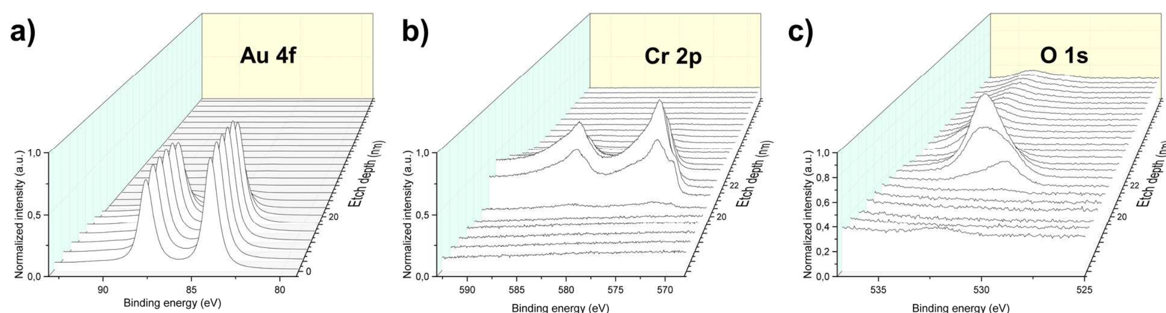

Figure 10. XPS peaks of the 2-Cr/20-Au sample XPS depth profiling on Si_3N_4 substrate. From the surface to a depth of 20 nm only the Au 4f signal is visible (a). XPS signals from deeper than 20 nm show the Au signal decrease and both Cr 2p (b) and O 1s (c) signals appear.

The Cr 2p peak fit (Fig. S6 Supplementary Information) is formed by three components: a metallic Cr doublet at 574.4 and 583.6 eV, a Cr_2O_3 doublet at 576.3 and 585.6 eV, and a CrO_3 doublet at 580 and 589.2 eV[17]. The result of the fit indicates the partial oxidation of Cr during the e-beam deposition process, as in the Ti case. The use of the same deposition conditions and of the same type of substrate with respect to Ti, and a similar chemical reactivity of Ti and Cr suggest that also the Cr layer gets further oxidized by the water and oxygen molecules present on the substrate surface.

A possible explanation for the Cr-Au enhanced adhesion is described in the following: similarly to Ti, also Cr is very reactive and reacts chemically both with the substrate and the Au over-layer after Au deposition. Cr_2O_3 has a higher enthalpy of formation with respect to TiO_2 (-1128 kJ/mol vs -945 kJ/mol)[25]. The standard enthalpy of formation of an element indicates the form in which the element is most stable at 1 atm of pressure: the more negative heat of formation, the higher is the affinity for oxygen. The high tendency for Cr to form an oxide leads to a high strength of the Cr-O chemical bond. Such strength might lead to an increase of the adhesion properties with respect to Ti, an advantage that can be used for the fabrication of devices having better mechanical properties. Furthermore, the higher diffusivity of Cr compared to Ti leads to a Cr-Au inter-diffusion for a limited thickness at the metal interface. At 50°C, the solubility of Cr in Au is around 5 at. %, while the solubility of Ti in Au is less than 1 at. % at 500°C[26,27]. One might speculate that due to the inter-diffusion, the number of Cr-Au bonds exceeds the number for the Ti-Au case, where the

1
2
3
4
5
6
7
8
9
10
11
12
13
14
15
16
17
18
19
20
21
22
23
24
25
26
27
28
29
30
31
32
33
34
35
36
37
38
39
40
41
42
43
44
45
46
47
48
49
50
51
52
53
54
55
56
57
58
59
60

chemical bonding can happen only at the surface interface, leading to a further adhesion increase in the Cr case.

Adhesion layer effect on bilayer thin-film electrical resistivity

The change in nanostructure of the Au thin-film due to the presence of an adhesion layer, shown above, has an important impact on the macroscopic properties such as electrical resistivity. Electrical resistivity in polycrystalline films is dependent on electron surface and grain boundary scattering, and we expect the grain size change measured with TKD to be reflected in the electrical properties. Furthermore, for the case of Cr adhesion layers, a Cr-Au alloy is formed, which also is expected to have an impact on the thin-film electrical resistivity. To investigate possible impacts, we measured the sheet resistance (R) of the three samples (20-Au, 2-Ti/20-Au, and 2-Cr/20-Au) investigated with TKD above using micro 4-point probe (μ4PP). Fig. 11a shows that the Ti/Au sample has a lower sheet resistance than pure Au which can be attributed to the two layers acting as parallel resistors[28]. Data normalization has been performed with respect to the average sheet resistance (R) measured at the 20-Au sample. To exclude tip wear effects of the μ4PP, the measurements were performed measuring with the same probe alternatively on the 20-Au and 2-Ti/20-Au sample, respectively. Moreover, to rule out thin-film thickness variation effects, Au TEM cross-section thickness measurements were performed on 36 points along the 20-Au and the 2-Ti/20-Au samples. They reveal a slightly thicker Au film thickness in the Ti/Au sample compared to the pure Au film (23.6 ± 0.5 nm vs 21.9 ± 0.5 nm, respectively). Since electrical resistivity is inversely proportional to film thickness, the thicker Au film contributes to decrease the sheet resistance in the Ti/Au sample with respect to pure Au. Fig. 11b shows that the Cr/Au system has a higher sheet resistance than pure Au. In this case, the formation of a single layer due to Cr-Au inter-diffusion compromises the multilayer assumption. The sheet resistance increase is in line with the general resistivity increase of chromium-gold alloys, which increase linearly with the Cr concentration[29]. Data acquisition and normalization have been done as in the Ti/Au case above, and TEM cross-section thickness measurements of the Au layer were done on 29 points

of the Cr/Au sample, giving a mean thickness of 22.7 ± 0.4 nm. Compared with the thickness of pure Au, this value is slightly higher. However, the sheet resistance decrease due to this thickness difference is not enough to compensate the increase due to the Cr-Au alloy formation.

The Ti/Au parallel behavior and Cr/Au inter-diffusion seems to have a bigger impact on the electrical properties of the multilayer systems than the nanostructure change observed by TKD. For both samples, the increase of grain boundary scattering due to the higher density of grain boundaries, compared to pure Au, could not be measured with our setup, but cannot be excluded a priori.

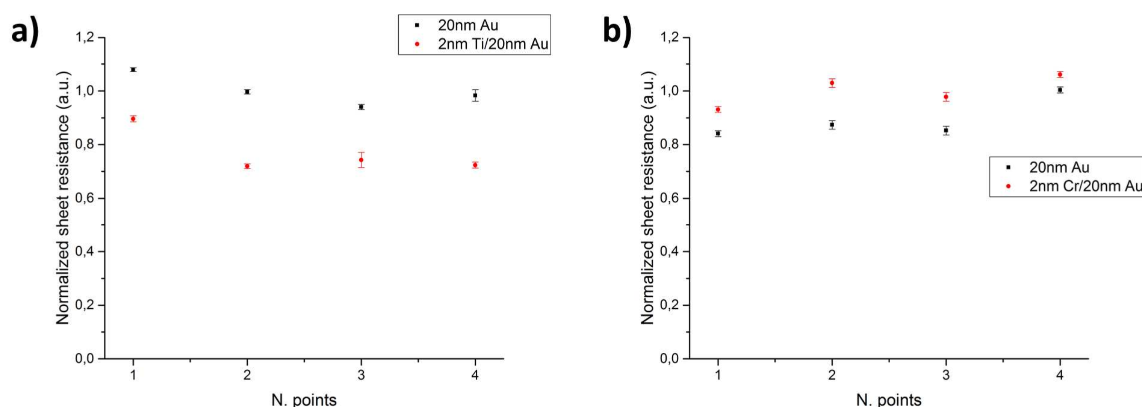

Figure 11. Normalized sheet resistance of: (a) 20-Au vs 2-Ti/20-Au samples; (b) 20-Au vs 2-Cr/20-Au samples. The Ti/Au bilayer system has lower sheet resistance than pure Au (a) due to parallel resistors behavior. The Cr/Au bilayer system has higher sheet resistance than pure Au (b) due to Cr-Au alloy formation.

Revised adhesion layer model

Based on the above results, we propose a revised adhesion layer model for Ti/Au and Cr/Au thin-film systems. The model is intended as an improvement in the description of the layer-layer interaction compared to the model described in the introduction. The model will help the thin-film engineering of nanodevices.

The adhesion layer model is shown in Fig. 12. The growth of both adhesion layers starts with the deposition of the atoms on the substrate (1) and the subsequent formation of an amorphous layer (2). During the

1 2 3 4 5 6 7 8 9 10 11 12 13 14 15 16 17 18 19 20 21 22 23 24 25 26 27 28 29 30 31 32 33 34 35 36 37 38 39 40 41 42 43 44 45 46 47 48 49 50 51 52 53 54 55 56 57 58 59 60

deposition, both Ti and Cr get partially oxidized by oxygen and water molecules present on the substrate surface and in the deposition chamber. The adhesion layer acts as a wetting layer for Au, reducing the nucleation energy barrier and increasing the number of nucleation sites compared to the pure Au case where Au is directly evaporated onto the SiO_2 surface. The enhanced wetting is due to the formation of Ti-Au and Cr-Au chemical bonds. This leads to the formation of a continuous film having i) monodisperse grain size and ii) the energetically most favorable [111] crystal orientation for Au (3). For the Cr/Au system there is an extra step: the inter-diffusion between Cr and Au to form a Cr-Au alloy (4). Such diffusion is limited to a thickness of 2-3 nm for samples prepared at room temperature.

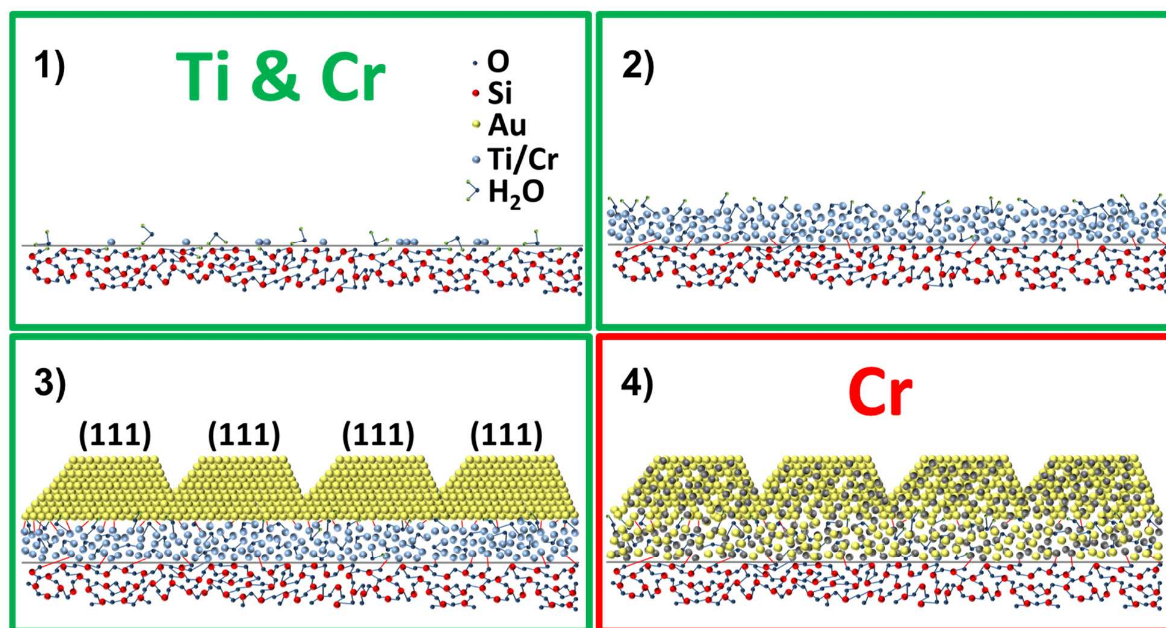

Figure 12. Revised adhesion layer model for Ti/Au and Cr/Au multilayer systems. (1) Adhesion layer nucleation; (2) growth of a partially oxidized adhesion layer; (3) growth of Au grains with [111] crystal orientation on top of the adhesion layer; (4) only for Cr: Cr/Au inter-diffusion and alloy formation during/after Au deposition.

Implications and recommendations for nanodevice fabrication

Our results have important implications for the nanofabrication of nano-optic and nano-electronic devices mentioned in the introduction. For nano-optic devices there are two implications. First, the grain size

1
2
3
4
5
6
7
8
9
10
11
12
13
14
15
16
17
18
19
20
21
22
23
24
25
26
27
28
29
30
31
32
33
34
35
36
37
38
39
40
41
42
43
44
45
46
47
48
49
50
51
52
53
54
55
56
57
58
59
60

values of the Au thin-films are comparable with the sizes of plasmonic nanostructures, which are 70-200 nm[30]. Hence, each nanostructure might have multi-grain structures that are different. This might affect its interaction with the light and its optical response, which leads to broadening of the optical resonance peaks. Second, during light and plasmonics device interactions, the temperature can locally raise to above 795 K[31], further enhancing the alloying of Cr and Au already present at room temperature and thus deteriorating the electrical properties of the thin-film stack. Ti does not inter-diffuse with Au at room temperature, supported by the µ4PP measurements which show that the electrical properties appear to be similar to pure Au thin-films. The formation of a stable Ti layer under the Au prevents diffusion of Au into the underlying substrate and improves the performance-time and temperature stability of the devices. The Ti-Au inter-diffusion starts at temperatures higher than 175°C. If the devices have to be used for prolonged time above this temperature, Pd[19] and Pt[21.22] diffusion barriers must be used.

Comparative studies show a localized surface plasmon damping in plasmonic nanostructures due to the presence of a very thin adhesion layer, and overall better performances of Ti over Cr for the optical resonance of such nanostructures[32–34]. Therefore, if the choice is limited to metallic adhesion layers, Ti is preferred over Cr for nano-optics applications. A perhaps even better alternative is to use organosilane-based adhesion layers. Comparative measurements of Ti versus MPTMS[35] and Cr versus APTMS[36] show overall better performances for the organosilane-based adhesion layers over the metallic ones. The big disadvantage of these molecular adhesion layers is their lack of compatibility with the lithographic and lift-off processes, which still play an important role in the fabrication of nanostructures.

For nano-electronics applications, our results show that Ti and Cr form oxides with surface adsorbed water and free oxygen in the vacuum chamber of the physical vapor deposition system. To avoid oxidation of the adhesion layer, the chamber vacuum needs to be in UHV conditions and the sample must be baked to remove the surface adsorbed water. However, these baking temperatures are not compatible with e.g. lift-off nanofabrication of nano-electronic devices that often utilize photo or electron beam lithography resists which do not tolerate high baking temperatures. In the case of carbon nanotubes (CNTs), Ti uniformly coats

1 2 3 4 5 6 7 8 9 10 11 12 13 14 15 16 17 18 19 20 21 22 23 24 25 26 27 28 29 30 31 32 33 34 35 36 37 38 39 40 41 42 43 44 45 46 47 48 49 50 51 52 53 54 55 56 57 58 59 60

the nanotube surface[37]. That implies that the partially oxidized Ti uniformly coats CNTs, which might lead to poor electrical contact to the nano-electronic device. However, it is unclear if this is true for other nano-electronics materials, because their surface chemistry is different. To avoid oxidation of Ti or Cr that is in physical contact with the nano-electronic materials, one solution is to avoid these materials completely. Indeed, some of the best performing CNT devices are made without the use of adhesion layers, as e.g. Pd which is directly used[38]. For MoS_2 FETs, Radisavljevic showed that pure Au contacts out-performed Ti/Au contacts[39]. If an adhesion layer is required for mechanical stability, a less than 2-nm-thin Cr layer is recommended, and Ti must be avoided. This is because the partially oxidized Ti might form a barrier between the nano-electronic material and the Au over-layer, with a consequent deterioration of the electron transport performances. Because of the single-layer morphology due to the Cr-Au alloy formation, the alloy will make electrical and physical contact to the nano-electronic material, despite the chrome oxide content. Furthermore, a low temperature annealing will enhance inter-diffusion of Au and Cr, and improve electrical contact between the nano-electronic material and the Au over-layer. Indeed, low temperature annealing is often used in nano-electronic fabrication for improving electrical contact[39,40]. Finally, an important implication is that better adhesion layers for nano-electronics might be metals with electrically conductive oxides such as ruthenium and iridium[41,42].

CONCLUSIONS

We have investigated the influence of Ti and Cr adhesion layers on ultra-thin Au films using complementary characterization techniques. The thin-film stacks are deposited by electron beam evaporation at room temperature. Profound morphological differences have been observed: Ti forms a continuous layer below Au, while Cr and Au show inter-diffusion. Both adhesion layers have an impact on the Au texture, with the formation of thin-films having smaller grain sizes than pure Au. All thin-films have [111] crystal orientation. Both Ti and Cr are partially oxidized during the thin-film deposition, and the oxygen source is molecular oxygen and water molecules adsorbed onto the substrate surface and from the environment in the

1 2 3 4 5 6 7 8 9 10 11 12 13 14 15 16 17 18 19 20 21 22 23 24 25 26 27 28 29 30 31 32 33 34 35 36 37 38 39 40 41 42 43 44 45 46 47 48 49 50 51 52 53 54 55 56 57 58 59 60

deposition chamber. Electrical measurements show an electrical conductivity increase for Ti/Au and deterioration for Cr/Au stacks compared to pure Au. This result is attributed to film parallel resistor behavior for Ti/Au, and Cr/Au alloy formation, respectively. These effects have a larger impact on the electrical properties of the multilayer systems than the nanostructure change due to the adhesion layer presence, which however cannot be excluded. Based on our results, we propose a revised adhesion model for the Ti/Au and Cr/Au multilayer systems, which gives a description of the adhesion layer-overlayer interaction and can be used by the research community as guide-lines for adhesion layer and thin-film stack engineering. To conclude, we recommend the use of Ti adhesion layers for nano-optics applications, thanks to its low diffusion, time stability and compatibility with lift-off procedures. If nano-lithography and lift-off is not required, organosilane-based adhesion layers are superior to metallic adhesion layers. For nano-electronic devices, adhesion layers should be avoided because of possible oxide barrier formation. If adhesion layers are needed for mechanical stability, Cr is preferred, thanks to Cr-Au alloy formation, which implies a superior electrical and physical contact to the nano-electronic material.

METHODS

FILM DEPOSITION

Ti, Cr and Au films have been deposited by e-beam evaporation using a Wordentec QCL 800 deposition machine (Wordentec Limited, Shebbear, UK). The films have been deposited with a deposition rate of 1 Å/s, chamber pressure of $3 \cdot 10^{-6}$ mbar and substrate temperature between 17 and 20°C. The thin-film thickness has been measured by the use of a quartz crystal thickness monitor (QCM). Samples for µ4PP and TKD have been deposited on 5–nm-thickness Si_3N_4 TEM grids (Caspilor AB, Lidingö, Sweden) using a special sample holder designed specifically to fit into the 100 mm wafer holder of the deposition machine. Samples for TEM cross section studies (bright field imaging, AFM, EDX, EELS) have been deposited on 100 mm silicon wafers coated with 110-nm thick thermally grown amorphous SiO_2. Samples for XPS have been deposited on silicon wafers coated with 150-nm-thick amorphous Si_3N_4 grown by low-pressure chemical vapor

1 2 3 4 5 6 7 8 9 10 11 12 13 14 15 16 17 18 19 20 21 22 23 24 25 26 27 28 29 30 31 32 33 34 35 36 37 38 39 40 41 42 43 44 45 46 47 48 49 50 51 52 53 54 55 56 57 58 59 60

deposition (LPCVD). Before thin-film deposition, the substrates were treated with an oxygen plasma for 5 min.

FOCUSED ION BEAM MILLING

TEM cross section samples have been prepared using focused ion beam (FIB) milling inside a FEI Helios Nanolab 600 FIB-SEM (FEI Company, Hillsboro OR, USA). From the original silicon wafer substrates, 1 cm^2 area chips have been cut out and glued on standard SEM stubs. Silver paste was used to electrically connect the chips with the stub. A 2-µm-thick C-Pt layer was deposited as film protection on the top surface of the chips. It was deposited by a combination of electron beam induced deposition (EBID) and ion beam induced deposition (IBID). From the chips, a thin cross-section lamella was milled out. The lamella was then lifted out by a dedicated micromanipulator and fixed onto a Cu TEM half-grid placed inside the FIB chamber. The fixation was performed using C-Pt IBID. The final FIB for electron-transparent thinning was performed with the lamella on the TEM grid. The FIB-SEM was operated at 30 kV for ion processing, with ion current ranging between 26 pA (for imaging) and 9 nA (for rough milling). The SEM imaging was performed at 5 kV.

TRANSMISSION ELECTRON MICROSCOPY

TEM bright field images have been acquired using a FEI Tecnai T20 G2 TEM operated at 200 kV. HR-STEM, EDX and EELS data have been acquired using a monochromated and probe corrected FEI Titan Analytical 80-300ST TEM. The instrument was operated at an accelerating voltage of 300 kV, probe convergence angle of 35 mrad, EELS collection angle of 16 mrad, and with a resulting imaging resolution of 1 Å and energy resolution of 1 eV. The sample is aligned with respect to the electron optical axis in order to have the Si (100) plane parallel to the electron beam.

ATOMIC FORCE MICROSCOPY

1 2 3 4 5 6 7 8 9 10 11 12 13 14 15 16 17 18 19 20 21 22 23 24 25 26 27 28 29 30 31 32 33 34 35 36 37 38 39 40 41 42 43 44 45 46 47 48 49 50 51 52 53 54 55 56 57 58 59 60

AFM measurements have been performed using a Dimension Icon-PT system (Bruker Corporation, Billerica, MA, USA). Peak force modulation was used. The acquisition parameters were 500 nm scan size, 0.977 Hz scan rate and 512 samples for each line. The AFM probes have a nominal tip radius of 2 nm, 70 kHz resonant frequency and 0.4 N/m spring constant.

TRANSMISSION KIKUCHI DIFFRACTION

TKD patterns have been acquired with a FEI Nova 600 NanoSEM equipped with an OPTIMUS TKD detector head (Bruker Corporation, Billerica, MA, USA). The patterns were analyzed using both CrystAlign (Bruker) and OIM TSL analysis software. In order to decrease sample contamination observed in high vacuum mode and to avoid sample drift, low vacuum mode was used. The acquisition parameters were 30 kV electron accelerating voltage, 2 nA current and 3 nm beam step size. To determine the average grain size, the data were processed to remove wrong-indexed points and to define a grain. A grain was defined as an area containing at least 3 data points with the same orientation and with a misorientation larger than 2° to its neighbour. All data sets containing less than 3 points were removed from the maps, due to uncertainty in the indexing and are shown as black areas.

X-RAY PHOTOELECTRON SPECTROSCOPY

XPS depth profiles have been performed using a ThermoScientific K-alpha XPS (Thermo Fisher Scientific, Waltham MA, USA), having an Al K-α 1486.7 eV X-ray source and a 3 kV Ar ion gun. The X-ray spot size was 400 µm, the etch step time was 15 s and the energy step size was 0.05 eV. Each spectrum was acquired as an average of 10 scans. XPS chemical trace analysis was performed using Thermo Avantage v5.948 software from ThermoScientific.

MICRO-4 POINT PROBE

1
2
3
4
5
6
7
8
9
10
11
12
13
14
15
16
17
18
19
20
21
22
23
24
25
26
27
28
29
30
31
32
33
34
35
36
37
38
39
40
41
42
43
44
45
46
47
48
49
50
51
52
53
54
55
56
57
58
59
60

Sheet resistance has been measured inside a FEI Nova 600 NanoSEM equipped with a MM3A-EM micromanipulator (Kleindiek Nanotechnik GmbH, Reutlingen, Germany) and a μ4PP micro four-point probe plug-in (Capres A/S, Kongens Lyngby, Denmark). Aided by SEM imaging, the probe gently touched the thin-film surface in 2-point probe mode without scratching it. Data were collected in 4-point probe mode using an M4PP SEM MODULE from Capres A/S. Acquisition parameters included 30 μA current, 100 gain, 390.6 Hz, and 82 ms integration time. 1000 data points were collected per measurement point. Four measurements were executed for each sample.

AUTHOR INFORMATION

Corresponding author: Anpan Han.

*Email: anph@dtu.dk

ACKNOWLEDGEMENTS

We thank the DTU Danchip CEN staff for instrument support.

SUPPORTING INFORMATION

The material presented in the Supporting Information includes further analysis of the pure Au, Ti/Au and Cr/Au bilayer samples. The data include AFM images of the analyzed cross-section samples, high resolution TEM cross section of Ti/Au sample, XPS depth profile of a Ti/Au multilayer system and XPS peak fits of Ti and Cr peaks. A paragraph is dedicated to the description of thin-film crystal growth more in detail.

REFERENCES

(1) Zhao, H.; Wang, C.; Vellacheri, R.; Zhou, M.; Xu, Y.; Fu, Q.; Wu, M.; Grote, F.; Lei, Y. Self-Supported Metallic Nanopore Arrays with Highly Oriented Nanoporous Structures as Ideally Nanostructured

1
2
3
4
5
6
7
8
9
10
11
12
13
14
15
16
17
18
19
20
21
22
23
24
25
26
27
28
29
30
31
32
33
34
35
36
37
38
39
40
41
42
43
44
45
46
47
48
49
50
51
52
53
54
55
56
57
58
59
60

Electrodes for Supercapacitor Applications. *Adv. Mater.* **2014**, *26*, 7654–7659.

(2) Wei, R.; Gatterdam, V.; Wieneke, R.; Tampé, R.; Rant, U. Stochastic Sensing of Proteins with Receptor-Modified Solid-State Nanopores. *Nat. Nanotechnol.* **2012**, *7*, 257–263.

(3) Zhu, Y. F.; Lang, X. Y.; Zheng, W. T.; Jiang, Q. Electron Scattering and Electrical Conductance in Polycrystalline Metallic Films and Wires: Impact of Grain Boundary Scattering Related to Melting Point. *ACS Nano* **2010**, *4*, 3781–3788.

(4) Wu, W.; Brongersma, S. H.; Van Hove, M.; Maex, K. Influence of Surface and Grain-Boundary Scattering on the Resistivity of Copper in Reduced Dimensions. *Appl. Phys. Lett.* **2004**, *84*, 2838–2840.

(5) Zhang, Q. G.; Cao, B. Y.; Zhang, X.; Fujii, M.; Takahashi, K. Influence of Grain Boundary Scattering on the Electrical and Thermal Conductivities of Polycrystalline Gold Nanofilms. *Phys. Rev. B - Condens. Matter Mater. Phys.* **2006**, *74*, 134109.

(6) Keller, R. R.; Geiss, R. H. Transmission EBSD from 10 Nm Domains in a Scanning Electron Microscope. *J. Microsc.* **2012**, *245*, 245–251.

(7) Fundenberger, J. J.; Bouzy, E.; Goran, D.; Guyon, J.; Yuan, H.; Morawiec, A. Orientation Mapping by Transmission-SEM with an on-Axis Detector. *Ultramicroscopy* **2016**, *161*, 17–22.

(8) Petrov, I.; Barna, P. B.; Hultman, L.; Greene, J. E. Microstructural Evolution during Film Growth. *J. Vac. Sci. Technol. A* **2003**, *21*, S117.

(9) Messier, R. Revised Structure Zone Model for Thin Film Physical Structure. *J. Vac. Sci. Technol. A*, **1984**, *2*, 500.

(10) Jach, T.; Hembree, G.; Holdeman, L. B. Observation of Gold Thin Film Growth with Reflection Electron Microscopy. *Thin Solid Films* **1990**, *187*, 133–140.

(11) Erdogdu, Y.; Jian, T.; Lopez, G. V.; Li, W. L.; Wang, L. S. On the Electronic Structure and Chemical Bonding of Titanium Tetraauride: TiAu4 and TiAu4-. *Chem. Phys. Lett.* **2014**, *610–611*, 23–28.

(12) Brewer, L. A Bonding Model for Strong Generalized Lewis Acid-Base Interactions in Intermetallics.

1
2
3
4
5
6
7
8
9
10
11
12
13
14
15
16
17
18
19
20
21
22
23
24
25
26
27
28
29
30
31
32
33
34
35
36
37
38
39
40
41
42
43
44
45
46
47
48
49
50
51
52
53
54
55
56
57
58
59
60

Pure Appl. Chem. **1988**, *60*, 281–286.

(13) Anders, A.; Byon, E.; Kim, D. H.; Fukuda, K.; Lim, S. H. N. Smoothing of Ultrathin Silver Films by Transition Metal Seeding. *Solid State Commun.* **2006**, *140*, 225–229.

(14) Fukuda, K.; Lim, S. H. N.; Anders, A. Coalescence of Magnetron-Sputtered Silver Islands Affected by Transition Metal Seeding (Ni, Cr, Nb, Zr, Mo, W, Ta) and Other Parameters. *Thin Solid Films* **2008**, *516*, 4546–4552.

(15) Logeeswaran, V. J.; Kobayashi, N. P.; Islam, M. S.; Wu, W.; Chaturvedi, P.; Fang, N. X.; Wang, S. Y.; Williams, R. S. Ultrasmooth Silver Thin Films Deposited with a Germanium Nucleation Layer. *Nano Lett.* **2009**, *9*, 178–182.

(16) Formica, N.; Ghosh, D. S.; Carrilero, A.; Chen, T. L.; Simpson, R. E.; Pruneri, V. Ultrastable and Atomically Smooth Ultrathin Silver Films Grown on a Copper Seed Layer. *ACS Appl. Mater. Interfaces* **2013**, *5*, 3048–3053.

(17) Alexander, N.; Anna, K.-V.; Stephen, G.; Cedric, P. NIST X-ray Photoelectron Spectroscopy Database https://srdata.nist.gov/xps/Default.aspx.

(18) Masahiro, K.; Noboru, S. Effects of Temperature, Thickness and Atmosphere on Mixing in Au-Ti Bilayer Thin Films. *J. Mater. Sci.* **1993**, *28*, 5088–5091.

(19) Tisone, T. C.; Drobek, J. Diffusion in Thin Film Ti–Au, Ti–Pd, and Ti–Pt Couples. *J. Vac. Sci. Technol.* **1972**, *9*, 271.

(20) Hieber, H. Aging Properties of Gold Layers with Different Adhesion Layers. *Thin Solid Films* **1976**, *37*, 335–343.

(21) Lepselter, M. P. Beam-Lead Technology. *Bell Syst. Tech. J.* **1966**, *45*, 233–253.

(22) Pan, J.; Pafchek, R. M.; Judd, F. F.; Baxter, J.; Obispo, S. L. Effect of Chromium-Gold and Titanium-Titanium Nitride-Platinum-Gold Metallization on Wire / Ribbon Bondability. **2004**, 3–8.

(23) Vancea, J.; Reiss, G.; Schneider, F.; Bauer, K.; Hoffmann, H. Substrate Effects on the Surface Topography of Evaporated Gold Films-A Scanning Tunnelling Microscopy Investigation. *Surf. Sci.*

1989, *218*, 108–126.

(24) Werner, W. S. M. Towards a Universal Curve for Electron Attenuation: Elastic Scattering Data for 45 Elements. *Surf. Interface Anal.* **1992**, *18*, 217–228.

(25) Zumdahl, S. S. Chemical Principles. *Vasa*, **2005**, 1–1183.

(26) Murray, J. L. The Au-Ti (Gold-Titanium) System. *Bull. Alloy Phase Diagrams* **1983**, *4*, 278–283.

(27) Okamoto, H.; Massalski, T. B. The Au-Cr (Gold-Chromium) System. *Bull. Alloy Phase Diagrams* **1985**, *6*, 224–228.

(28) Chen, Y.-Y.; Juang, J.-Y. Finite Element Analysis and Equivalent Parallel-Resistance Model for Conductive Multilayer Thin Films. *Meas. Sci. Technol.* **2016**, *27*, 74006.

(29) Slusark, W.; Lalevic, B.; Fuschillo, N. Structure and Electrical Conductivity of Cosputtered Gold-Chromium Alloy Films. *J. Appl. Phys.* **1973**, *44*, 2891–2892.

(30) Schuller, J. A.; Barnard, E. S.; Cai, W.; Jun, Y. C.; White, J. S.; Brongersma, M. L. Plasmonics for Extreme Light Concentration and Manipulation. *Nat. Mater.* **2010**, *9*, 193–204.

(31) Chen, X.; Chen, Y.; Yan, M.; Qiu, M. Nanosecond Photothermal Effects in Plasmonic Nanostructures. *ACS Nano* **2012**, *6*, 2550–2557.

(32) Jiao, X.; Goeckeritz, J.; Blair, S.; Oldham, M. Localization of near-Field Resonances in Bowtie Antennae: Influence of Adhesion Layers. *Plasmonics* **2009**, *4*, 37–50.

(33) Najiminaini, M.; Vasefi, F.; Kaminska, B.; Carson, J. J. L. Optical Resonance Transmission Properties of Nano-Hole Arrays in a Gold Film: Effect of Adhesion Layer. *Opt. Express* **2011**, *19*, 26186.

(34) Aouani, H.; Wenger, J.; Gérard, D.; Rigneault, H.; Devaux, E.; Ebbesen, T. W.; Mahdavi, F.; Xu, T.; Blair, S. Crucial Role of the Adhesion Layer on the Plasmonic Fluorescence Enhancement. *ACS Nano* **2009**, *3*, 2043–2048.

(35) Habteyes, T. G.; Dhuey, S.; Wood, E.; Gargas, D.; Cabrini, S.; Schuck, P. J.; Alivisatos, A. P.; Leone, S. R. Metallic Adhesion Layer Induced Plasmon Damping and Molecular Linker as a Nondamping Alternative. *ACS Nano* **2012**, *6*, 5702–5709.

1
2
3
4
5
6
7
8
9
10
11
12
13
14
15
16
17
18
19
20
21
22
23
24
25
26
27
28
29
30
31
32
33
34
35
36
37
38
39
40
41
42
43
44
45
46
47
48
49
50
51
52
53
54
55
56
57
58
59
60

(36) Sukham, J.; Takayama, O.; Lavrinenko, A. V.; Malureanu, R. High-Quality Ultrathin Gold Layers with an APTMS Adhesion for Optimal Performance of Surface Plasmon-Polariton Based Devices. *ACS Appl. Mater. Interfaces* **2017**, acsami.7b07181.

(37) Zhang, Y.; Dai, H. Formation of Metal Nanowires on Suspended Single-Walled Carbon Nanotubes. *Appl. Phys. Lett.* **2000**, *77*, 3015–3017.

(38) Javey, A.; Guo, J.; Wang, Q.; Lundstrom, M.; Dai, H. Ballistic Carbon Nanotube Field-Effect Transistors. *Nature* **2003**, *424*, 654–657.

(39) Radisavljevic, B.; Radenovic, A.; Brivio, J.; Giacometti, V.; Kis, A. Single-Layer MoS2 Transistors. *Nat. Nanotechnol.* **2011**, *6*, 147–150.

(40) Han, A.; Vlassarev, D.; Wang, J.; Golovchenko, J. A.; Branton, D. Ice Lithography for Nanodevices. *Nano Lett.* **2010**, *10*, 5056–5059.

(41) Vayunandana Reddy, Y. K.; Mergel, D. Structural and Electrical Properties of RuO2 Thin Films Prepared by Rf-Magnetron Sputtering and Annealing at Different Temperatures. *J. Mater. Sci. Mater. Electron.* **2006**, *17*, 1029–1034.

(42) Liu, Y.; Masumoto, H.; Goto, T. Electrical and Optical Properties of IrO2 Thin Films Prepared by Laser-Ablation. *Mater. Trans.* **2004**, *45*, 3023–3027.

TOC GRAPHIC